

PAPER • OPEN ACCESS

# On the interaction between the island divertor heat fluxes, the scrape-off layer radial electric field and the edge turbulence in Wendelstein 7-X plasmas










To cite this article: E. Maragkoudakis *et al* 2023 *Nucl. Fusion* **63** 026011

View the [article online](#) for updates and enhancements.

You may also like

- [Peripheral temperature gradient screening of high-Z impurities in optimised 'hybrid' scenario H-mode plasmas in JET-ILW](#)  
A.R. Field, F.J. Casson, D. Fajardo et al.
- [Effects of drifts on scrape-off layer transport in W7-X](#)  
D.M. Kriete, A. Pandey, V. Perseo et al.
- [Rational surfaces, flows and radial structure in the TJ-II stellarator](#)  
B.Ph. van Milligen, I. Voldiner, B.A. Carreras et al.

# On the interaction between the island divertor heat fluxes, the scrape-off layer radial electric field and the edge turbulence in Wendelstein 7-X plasmas

E. Maragkoudakis<sup>1,a,\*</sup> , D. Carralero<sup>1</sup> , T. Estrada<sup>1</sup> , T. Windisch<sup>2</sup>, Y. Gao<sup>2</sup> , C. Killer<sup>2</sup> , M. Jakubowski<sup>2</sup> , A. Puig Sitjes<sup>2</sup>, F. Pisano<sup>3</sup>, H. Sándor<sup>4</sup>, M. Vecsei<sup>4</sup> , S. Zoletnik<sup>4</sup> , A. Cappa<sup>1</sup>  and the W7-X Team<sup>a</sup>

<sup>1</sup> Laboratorio Nacional de Fusión, CIEMAT, 28040 Madrid, Spain

<sup>2</sup> Max-Planck-Institut für Plasmaphysik, D-17491 Greifswald, Germany

<sup>3</sup> Department of Electrical and Electronic Engineering, University of Cagliari, 09124 Cagliari, Italy

<sup>4</sup> Fusion Plasma Physics Department, Centre for Energy Research, 1121 Budapest, Hungary

E-mail: [emmanouil@ciemat.es](mailto:emmanouil@ciemat.es)

Received 30 September 2022, revised 13 November 2022

Accepted for publication 29 November 2022

Published 28 December 2022



## Abstract

The formation of the radial electric field,  $E_r$  in the scrape-off layer (SOL) has been experimentally studied for attached divertor conditions in stellarator W7-X. The main objective of this study is to test the validity in a complex three-dimensional (3D) island divertor of simple models, typically developed in tokamaks, relating  $E_r$  in the SOL to the sheath potential drop gradient at the target. Additionally, we investigate the effect of the edge  $E_r$  shear on the reduction of density fluctuation amplitude, a well-established phenomenon according to the existing bibliography. The main diagnostic for measurements in the SOL is a V-band Doppler reflectometer that can provide the measurement of the  $E_r$  and density fluctuations with good spatial resolution. 3D measurements of divertor parameters have been carried out using infrared cameras, with the exponential decay length of the divertor heat flux ( $\lambda_q$ ) resulting in a suitable proxy for the model-relevant  $\lambda_T$ , the exponential decay length of the temperature at the divertor. In the investigated attached regimes, it is shown for the first time that the formation of the  $E_r$  in the SOL depends on parameters at the divertor, following a  $E_r \propto T_e/\lambda_q$  qualitatively similar to that found in a tokamak. Then, from the analyzed plasmas, the observed  $E_r$  shear at the edge is linked to a moderate local reduction of the amplitude of density fluctuations.

Keywords: Doppler reflectometry, stellarator, SOL, Wendelstein 7-X

(Some figures may appear in colour only in the online journal)

<sup>a</sup> See Sunn Pedersen *et al* 2022 (<https://doi.org/10.1088/1741-4326/ac2cf5>) for the W7-X Team.

\* Author to whom any correspondence should be addressed.



Original Content from this work may be used under the terms of the [Creative Commons Attribution 4.0 licence](https://creativecommons.org/licenses/by/4.0/). Any further distribution of this work must maintain attribution to the author(s) and the title of the work, journal citation and DOI.

## 1. Introduction

The region surrounding the nested magnetic surfaces of a magnetic confinement device is truly important for the realistic development of a commercial fusion reactor, as it determines how the particle and energy fluxes are deposited onto the various surfaces facing the plasma. This region is typically referred to as the scrape-off layer (SOL) and can feature various degrees of complexity: from the relatively simple and symmetric SOL of a divertor tokamak, to the asymmetric geometry of a stellarator equipped with an island divertor involving an island chain with secondary regions around the O-points. A simple and general first approach is that SOL flows follow the open field lines onto the material surfaces that intersect them. However, this parallel transport must be compounded with substantial cross-field flows, typically referred to as ‘drifts’. Among them, perhaps the most important for SOL flows is the  $v_{E \times B}$  drift, caused by local gradients in electrostatic potential,  $\phi$ . These drifts may strongly influence the position and intensity of heat loads onto divertor targets [1] and have been proposed in the literature as the underlying mechanism for the observed asymmetries between the high field side and low field side divertors in tokamaks (see e.g. [2] and references therein). Because of this, a good understanding of the process of electric field formation in the SOL is of paramount importance for the optimized Helias stellarator Wendelstein 7-X (W7-X) [3–5]. This device, the largest of its kind currently in operation, achieved its first plasmas in 2016 [5] and has among its main objectives to test the island divertor as a valid plasma-wall interaction solution for a Helias reactor [6]. Besides its importance for SOL flows, the electric field in the SOL may also play a relevant role in the confinement and performance of the plasma in the region of closed flux surfaces, also referred to as region of confined plasma: typical W7-X plasmas feature a sheared  $E_r$  in the edge, as the negative ion root radial electric field in the confined region switches to the positive values usually found in the SOL. This creates a strong shear in the perpendicular  $v_{E \times B}$  velocity, which has been predicted to suppress turbulence and lead to the formation of transport barriers [7]. The structure of the radial electric field around the Last Closed Flux Surface (LCFS) has been found to play a key role in the transition to the improved confinement H-mode in tokamaks [8–10] and stellarators [11, 12] (although in some cases this  $E_r$  has been found to be the result rather than the cause of the transition [13, 14]). The majority of these studies have focused mainly on the negative branch of the radial electric field found in the confined region. However, a number of recent works suggest that the  $E_r$  value at the SOL might also have a direct impact on global confinement, either by setting the flow boundary condition at the SOL [15] or by enhancing the velocity shear and the suppression of edge turbulence [16]. In the latter case, a feedback mechanism is proposed which would link pedestal, SOL and target: as turbulence in the edge is reduced by the  $E_r$  shear, so is perpendicular anomalous particle and heat transport at the SOL, which would reinforce the velocity shear initially suppressing

edge turbulence. Although no systematic study has been carried out on the effect of  $E_r$  shear on the turbulent transport in the edge of W7-X, there are some indications that it might be leading to the suppression of fluctuations [17]. Also an investigation of the experimental scenarios of the last W7-X campaign indicated that the edge shear of  $E_r$  is strongly influenced by the value of  $E_r$  at the SOL [18]. Therefore, investigating the link between the SOL  $E_r$  formation, targets and turbulence suppression is certainly relevant in this device.

The formation of SOL electric fields in tokamaks has been extensively studied in recent years and many works on this subject can be found in literature. As a result, some simplified models [19] have been found to reasonably describe mid-plane potential profiles and electric fields. In general, upstream potential ( $\phi_u$ ) at a given radial position  $r$  can be defined as

$$\phi_u(r, s) = \phi_s(r) + \int_0^s E_{\parallel}(r, s) ds \quad (1)$$

where  $s$  is the coordinate along the field line,  $s = 0$  corresponds to the sheath entrance and  $\phi_s(r)$  is the potential at the sheath entrance, which for a material with conductive surface can be usually approximated taking the potential drop at the sheath,  $\phi_s(r) \simeq 3 T_e(r)/e$ . Regarding the parallel electric field, it can be obtained from the momentum equation for electrons along the  $\mathbf{B}$  direction,

$$E_{\parallel} = \frac{j_{\parallel}}{\sigma_{\parallel}} + \frac{1}{en_e} \frac{\partial p_e}{\partial s} + 0.71 \frac{1}{e} \frac{\partial T_e}{\partial s} \quad (2)$$

where  $j_{\parallel}$  and  $\sigma_{\parallel}$  are the parallel current and electric conductivity and  $p_e$  is the electron pressure.

The simplest situation is found for low density, attached divertor conditions (the so called sheath limited regime). In this case, resistivity is low over the SOL ( $j_{\parallel}/\sigma_{\parallel} \simeq 0$ ). Pressure can be considered roughly constant along the field line ( $p_e \simeq \text{const}$ ). As well,  $T_e$  gradients parallel to the magnetic field tend to be small across the SOL. Thus, the rhs of equation (1) is dominated by the first term and  $\phi_u(r) \simeq \phi_s(r)$ . This means that, for low densities,  $v_{E \times B}$  is mostly poloidal as it is dominated by the radial component of the electric field ( $E_{r,u}$ ) which in turn, is determined by the gradient of the electron temperature in front of the target. Indeed, assuming an exponential decay of the temperature at the sheath entrance  $T_{e,s} \simeq T_{e,0} \exp(-r/\lambda_T)$ , the radial electric field can be expressed as:

$$E_{r,u} \equiv -\frac{\partial \phi_u}{\partial r} \simeq -\frac{3}{e} \frac{T_{e,s}}{\lambda_T}. \quad (3)$$

As the density at the separatrix is increased, this situation becomes more complex: first, in the conduction dominated regime significant gradients of  $T_e$  appear along the field line and as the recycling in the target increases, charge exchange and other atomic processes begin to drain momentum from the plasma flow. However, it is when detachment is significant that the simple low density picture loses its validity: as the heat fluxes onto the target are greatly reduced around the

strike point, electron temperatures at the target drop and their profile becomes substantially flatter. Eventually, collisionality is increased to the point in which the first term in the rhs of equation (2) becomes dominant and the parallel electric field is raised by parallel currents. In this new situation, potential differences appear between poloidally adjacent flux tubes, leading to poloidal electric fields and strong radial drifts. As a result, this dominant electric field is related to thermoelectric or Pfirsch–Schlüter return currents and no longer bound to the  $T_e$  gradients at the target.

This physical picture is generally consistent with recent experimental results from tokamak plasmas: on the one hand, the simple relation between upstream radial electric fields at the target expressed in equation (3) has been verified for attached plasmas in DIII-D [20], JET [21] and AUG [22]. Also, experiments carried out in detached plasmas have shown how  $\phi_u$  is dominated by the parallel current contribution of the  $E_{\parallel}$  thus making the SOL drifts to be dominated by the  $E_{\theta} \times B$  term,  $\theta$  being the poloidal direction. Examples can be found in DIII-D [20] and TCV [23] tokamaks. This kind of investigation is less frequently found in stellarators, where the precise mechanism leading to the formation of electric fields in the SOL is not as clear. The main reason for this is the fully three-dimensional topology of their SOL, which substantially increases the complexity of both experiments and theoretical models. Nevertheless, some investigations have been carried out in stellarators featuring island divertors which indicate that the underlying mechanisms behind SOL could be qualitatively similar to those in tokamaks. In [24], flows onto the targets were investigated in divertor island configurations at Wendelstein 7-AS. For densities below detachment, strong up-down asymmetric shifts of the ion saturation current and  $T_{e,s}$  peaks are observed which nearly reverse when magnetic field direction is inverted. This was interpreted as a strong indication of  $v_{E \times B}$  drifts dominating cross-field SOL flows, in good agreement with EMC3-EIRENE simulations, which found the electric field to be dominated by the radial component associated to the sheath potential gradient [25–27]. Interestingly, the impact of drifts is found to be stronger than in a tokamak divertor with the same plasma parameters due to the longer connection lengths. More recently, similar results were obtained in reversed field experiments carried out in W7-X [28]. In those experiments, for low density operation, strong up-down asymmetries were found on the radial positions of the strike lines and heat load distributions onto the targets, which could be attributed to poloidal drifts originating from dominant  $E_r$  fields. In good agreement with this, the asymmetries were again reversed when the direction of the magnetic field was changed. However, when the same measurements were carried for higher densities, up-down asymmetries became much weaker and a general inwards shift of the heat and particle flows was observed. This would be the result of a more complex drift structure, in which  $E_r$  is weakened by the shallower gradients of  $T_e$  at the targets and substantial parallel gradients of temperature, giving rise to non-negligible  $E_{\parallel}$ .

In this work, we set out to investigate the mechanism giving rise to the radial electric field at the SOL for W7-X and its link to the suppression of edge turbulence. For this, we carry out upstream radial electric field measurements at the vicinity of the separatrix using a Doppler Reflectometer (DR) and use a Field Line Tracing (FLT) code to follow the field lines projecting the measurement locations onto the corresponding target. Since this results in a complex two-dimensional (2D) projection, we then resort to infrared imaging in order to obtain a heat flux profile corresponding to the line of sight of the reflectometer. Applying this analysis to a database of discharges covering a range of plasmas in the attached divertor regime for a given magnetic configuration, we are able to find for the first time in a stellarator with island divertor configuration, direct evidence of the upstream-downstream interaction mechanism described in equation (3). Besides, using a wider database of Doppler reflectometry measurements, we show how the observed variation in  $E_r$  shear moderately decreases the amplitude of density fluctuations across the separatrix. The remainder of this paper is organized as follows: the experimental set up along with elements of the analysis method will be described in section 2. All results will be presented in section 3. Finally, the summary and discussion are given in section 4.

## 2. Experimental setup and methodology

### 2.1. Wendelstein 7-X scenarios

The experiments reported in this article were performed at the superconducting optimized Helias stellarator W7-X with major radius  $R = 5.5$  m, minor radius  $a = 0.5$  m and magnetic field on axis  $B_0 = 2.5$  T [5]. W7-X uses an Electron Cyclotron Heating (ECH) system of ten long-pulsed gyrotrons (each delivering 0.8 MW) [29]. In each of its five periods, W7-X uses a set of ten non-planar ('NPC') and four planar ('PC') superconductive coils in order to produce the confining magnetic field. Along one period, the plasma cross-section changes, starting from the triangular to the bean shape and back, meeting the periodic conditions at the boundaries. W7-X can employ a number of configurations [30]. In most relevant configurations, resonant magnetic islands form at the plasma boundary which are intersected by the divertor plates creating the island-divertor [31, 32]. This set of resonant magnetic islands surrounding the LCFS is created by the non-planar coils while extra control over the magnetic topology of the islands is achieved through the use of another set of copper coils, the control coils ('CC') [33, 34]. As will be explained later, this work concerns plasmas in the standard configuration of W7-X (also seen in literature as 'EJM'). For the standard configuration, a 5/5 island chain<sup>5</sup> is created around the LCFS. Those islands are intersected periodically by the divertor. In each of the five periods of W7-X, there are two divertor

<sup>5</sup> Meaning 5 islands that wind around the stellarator torus 5 times.

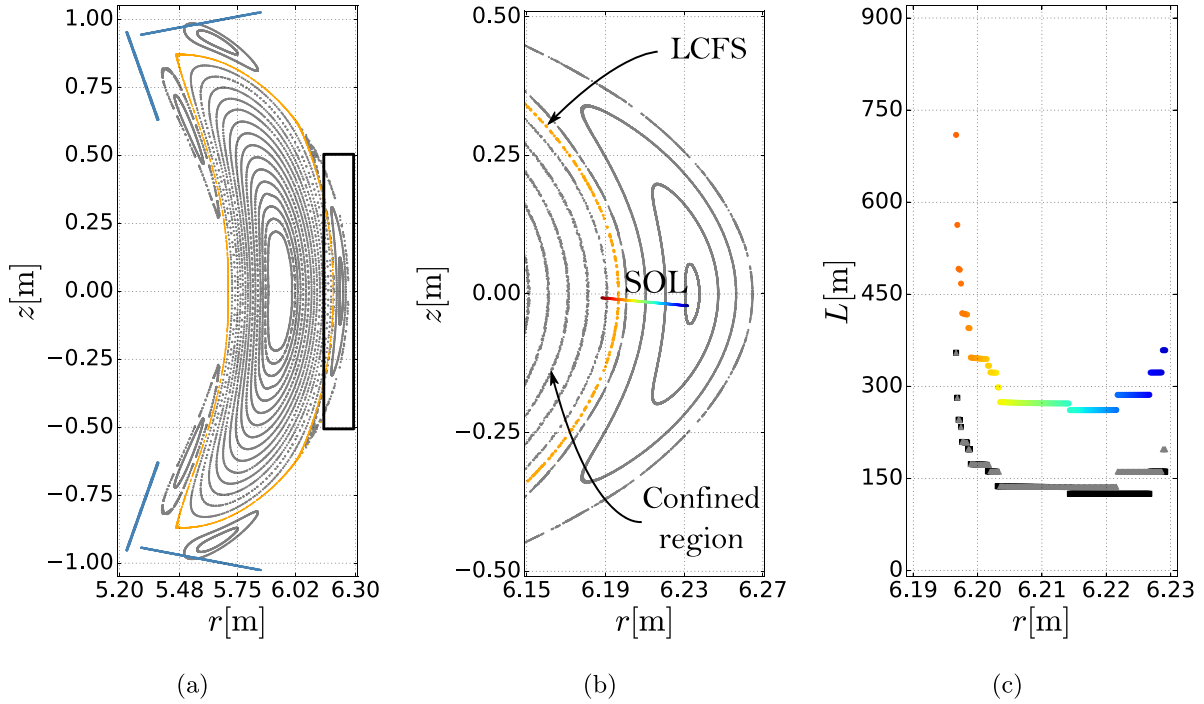


**Figure 1.** (a) Poincaré plot of the standard magnetic configuration of W7-X for toroidal angle of  $72^\circ$  (W7-X program 20 180 905.017,  $t = 4750\text{--}5000$  ms). The divertor target plates are depicted as blue lines, while the LCFS is depicted with orange color. The region inside the rectangle, also in (b), with the island crossing the mid-plane ( $z = 0$ ), is the region in which measurements are discussed later. The colored line represents the line of sight of the Doppler reflectometer in the SOL. In (c), the connection length calculated in the measurement area. Gray and black markers represent respectively the connection length to the target calculated in the parallel and anti-parallel direction to the magnetic field while their sum, the total connection length, is depicted with the colored markers.

modules, on the upper ('u') and the lower ('l') part. Each divertor module has two plates, the vertical ('v') and the horizontal ('h'). Thus, by referring to s1lh, we refer to module 1, lower horizontal target plate. For an in depth description of the island divertor concept, the reader is referred to [35].

The Poincaré plot of W7-X standard magnetic configuration at toroidal angle equal to  $72^\circ$  is obtained using an FLT code [36], which calculates the magnetic field using the Biot–Savart law using as input coil currents. The result is shown in figure 1(a): the 5/5 island chain is depicted outside the LCFS, which is indicated with orange color. For this toroidal angle, the magnetic field cross-section is bean-shaped and the divertor targets, depicted as blue diagonal lines, intersect the top and bottom islands. The island crossing the mid-plane ( $z = 0$ , in the rectangle) is drawn in more detail in figure 1(b). The colored line represents the line of sight of the DR, one of the main diagnostics used for this work that will be discussed later. As mentioned in the introduction, the higher the connection length of the island-divertor SOL field lines, the stronger the impact of drifts in the SOL transport. The field lines of the W7-X SOL have connection lengths of a few hundred meters [37], as can also be seen in figure 1(c), where the connection length to the target or other physical components ( $L$ ) was calculated along the line of sight of the DR. As well in the same plot, the SOL is defined as the region with values of  $L < 350$  m. For lower or higher values of the toroidal radial coordinate  $r$ , we encounter field lines of infinite  $L$  which correspond to the confined region inside of the LCFS or to the region in the vicinity

of the O-point of the island, the referred secondary confined regions.

## 2.2. Doppler reflectometry measurements

In order to investigate the topics presented in the introduction, we need to measure the  $E_r$  in the SOL, the density fluctuation amplitude and parameters over the divertor surface of W7-X. For the measurement of the radial electric field and the density fluctuation amplitude, we use the V-band monostatic frequency hopping Doppler reflectometer [38, 39]. The DR is installed at the AEA-21 port (toroidal angle  $72^\circ$ ). Its line of sight (depicted as colored line) is crossing the island of figure 1(b). A DR differs from conventional reflectometry in the finite angle between the probing wave and the cut-off layer normal, which is set in order to separate the Bragg back-scattered wave from the reflected wave at cut-off layer. By measuring the Doppler shifted back-scattered wave, the plasma turbulence and its perpendicular rotation velocity can be obtained. The latter is a composition of both the plasma  $E \times B$  velocity and the intrinsic phase velocity of the density turbulence:  $v_\perp = v_{E \times B} + v_{ph}$ . In cases in which the condition  $v_{E \times B} \gg v_{ph}$  holds, the radial electric field can be obtained directly from the perpendicular rotation velocity:  $E_r = B \cdot v_\perp = B \cdot 2\pi f_D / k_\perp$ , where  $f_D$  is the frequency of the Doppler peak and  $B$  is the magnetic field. Experiments performed in several devices have demonstrated that this assumption is, in general, valid [39–42], and only in high collisionality



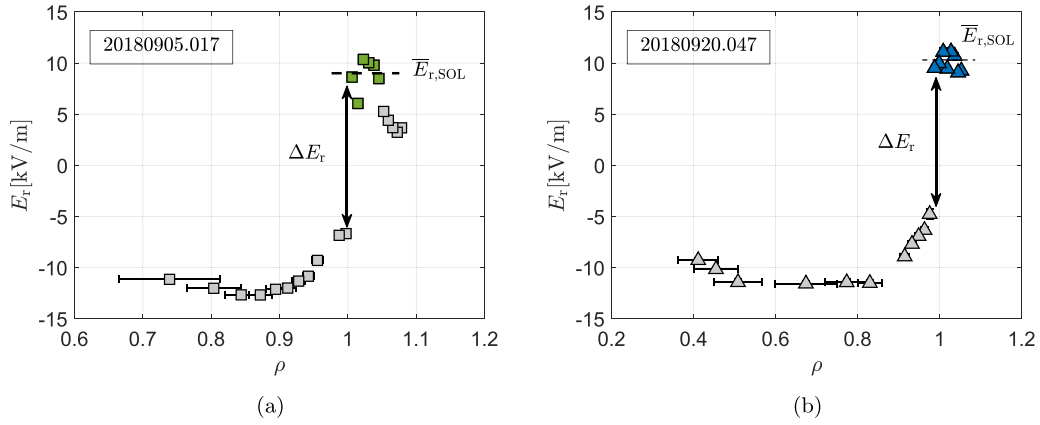


**Figure 2.** In (a) and (b), the radial electric field profile as given by the DR for program 20 180 905.017 ( $t = 4750$  ms to  $t = 5000$  ms) and 20 180 920.047 ( $t = 7000$  ms to  $t = 7250$  ms).

plasmas, the contribution of  $v_{ph}$  to  $v_{\perp}$  may become relevant [43, 44]. Besides, previous results obtained in W7-X show a good agreement between the experimental  $E_r$  profiles and those obtained from neoclassical predictions [18, 45]. Thus, it is sensible to assume that this condition holds also in the present experiments. Regarding the density fluctuations, the power of the back-scattered DR signal,  $S$ , is the relevant quantity proportional to  $\delta n_e^2$  and is given by  $S = A_D \cdot \Delta f_D$ , where  $A_D$  and  $\Delta f_D$  are the height and width of the Doppler peak. It has to be noted that, in general, a microwave generator working with variable frequency produces a different power output at each frequency. Besides, the transmitted power through the transmission line may also depend on the frequency. Therefore, a power calibration of the DR is indispensable for a proper comparison of the fluctuations measured at different frequencies.

For this work, the DR was programmed to use frequencies from 50 GHz to 74 GHz in ordinary mode polarization (O-mode) and with a fixed injection angle of  $18^\circ$ . A full frequency scan was set to last 250 ms with frequency steps of 1 GHz. For the calculation of the position of the cut-off and the  $k_{\perp}$  of the cut-off of the DR wave, we use the ray tracing code Travis [46] that takes as input the density profile and magnetic configuration. For this set-up, the expected values of  $k_{\perp}$  are between 7 and  $10 \text{ cm}^{-1}$ . Density measurements were provided by Thomson Scattering (TS) [47] and the mapping of those measurements along the flux surface coordinate  $\rho$  was calculated using VMEC equilibria [48]. For the estimation of uncertainties on the cut-off position and  $k_{\perp}$ , the reflection of a bundle of rays is considered in Travis, with a width equal to the  $1/e$  amplitude of the DR probing beam. Two typical examples of  $E_r$  profiles are shown in figure 2(a) for program 20 180 905.017 ( $t = 4750$  ms to  $t = 5000$  ms) and figure 2(b) for program 20 180 920.047 ( $t = 7000$  ms to  $t = 7250$  ms). These particular discharges are presented and used to show paradigmatic data from our database. A detailed explanation about the calculation of the vertical and horizontal uncertainty bars in the  $E_r$  profiles can be found in [18].

A few remarks on the DR data are in order: first, the DR can provide measurements for the region of open and closed field

lines. It was seen that there is a sufficient number of DR measurements in the SOL for plasmas with  $\bar{n}_e > 4.5 \times 10^{19} \text{ m}^{-3}$ . The transition from the SOL to the confined region inside the LCFS is seen in the DR signal as a sign reversal of the Doppler shift that regularly appears around the LCFS when the negative ion root  $E_r$  inside the LCFS [49, 50], changes to the positive  $E_r$  at the SOL, giving the rise to the observed velocity shear of the  $E_r$  at the edge. The variation of the  $E_r$  in this part of the plasma occurs in radial scales smaller than (a) the separation of the TS channels in this region [51] and (b) the radial resolution of the DR [52]. As a consequence, a point-by-point tracing of the  $E_r$  measurement points from the SOL to the divertor or the calculation of the radial derivative of  $E_r$  is not fully reliable. Thus, in this work, it is assumed that DR measurement points in the SOL lie on the line of sight of the antenna. This is a safe assumption considering that the refractive index in the SOL region does not cause the reflectometer beam to deviate significantly from the line of sight of the antenna, given the low local values of the density typically found in the island. This assumption has nevertheless been verified by Travis calculations.

In order to discuss the evolution of the SOL electric field, it is useful to define first an average value of the  $E_r$  in the SOL ( $\bar{E}_{r,SOL}$ ) as a uniform value along the measurement region and the variation of the radial electric field on the sign reversal ( $\Delta E_r$ ) as a proxy for the  $E_r$  shear. For the calculation of  $\bar{E}_{r,SOL}$ , we take the average for points with  $E_r > 0$ . While the observed values of  $\bar{E}_{r,SOL}$  are rather constant for most analyzed discharges (as in figure 2(b)), for plasmas with higher densities, the cut-off position moves outwards measuring a substantial decline of  $E_r$  across the SOL (example in figure 2(a)). In order to calculate  $\bar{E}_{r,SOL}$  in the most uniform manner, we use points close to the  $E_r$  sign reversal and ignore the ones corresponding to the referred decline. This is indicated in the examples in figure 2 by the colored markers in each plot: for 20 180 905.017,  $\bar{E}_{r,SOL}$  was found to be around  $9 \text{ kV m}^{-1}$  and for 20 180 920.047,  $\bar{E}_{r,SOL} \simeq 10 \text{ kV m}^{-1}$ ; depicted in the two figures as a dashed black horizontal line.  $\Delta E_r$  is calculated as the difference between the values of the radial electric field on

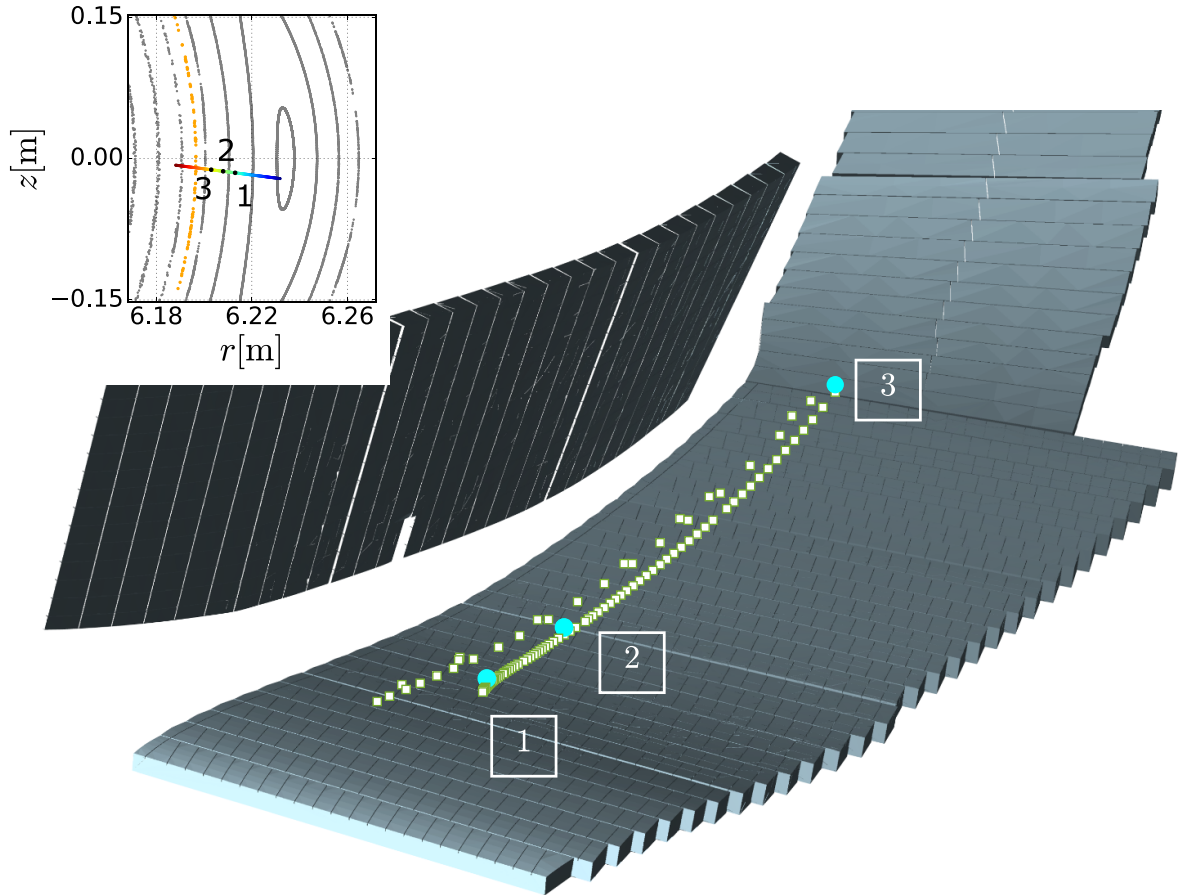


**Figure 3.** The ending points of the field line tracing with starting points from the measurement area from the upstream (seen in the supplementary figure) to the divertor target plates. The ending points lie over the 2D surface of the s11h target plate. For easier visualization of this projection from the SOL to the target numbered markers are used between the two plot. In the supplementary figure, the poloidal cross-section of 5/5 island of the standard configuration for program 20 180 905.017 ( $t = 4750\text{--}5000\text{ms}$ ) with the measurement area of the DR as colored line.

the sign reversal. It is found to be approximately  $15\text{ kV m}^{-1}$  for 20 180 905.017 and  $14\text{ kV m}^{-1}$  for 20 180 920.047 as indicated by a double vertical arrow in the two figures.

### 2.3. Field line tracing & heat fluxes on the target

An important part for this analysis is the connection of the measurement region in the SOL (figure 1(b)) with the divertor targets of the device along the magnetic field lines. The magnetic field lines are calculated using the aforementioned FLT. Aside the used currents of the NPC's and PC's, any non-negligible control coil current ( $I_{CC}$ ) and net toroidal current in the plasma ( $I_{tor}$ ) were also considered in the calculation of the magnetic field. In particular,  $I_{tor}$  was modeled as a current filament along the magnetic axis of the standard configuration. In order to make this calculation meaningful, discharges and times have been selected such that  $I_{tor}$  can be considered constant during one full DR frequency scan. For example, in the reference experiment 20 180 905.017, for 4750–5000ms  $I_{tor}$  has an average value of approximately 3.2kA with standard deviation that is  $\sim 40\text{A}$ . In figure 3, the s11h and s11v divertor target plates are depicted. The green markers that lie on its

surface represent the projection of the measurement area in the SOL. For easier identification and understanding of the projection of the measurement area on the target, three numbered markers are used for the two plots. As will be seen later, those markers also indicate the region of interest for the calculation of important parameters on the divertor. The ending points of the FLT lie all over the 2D surface of the target and do not align with the radial or toroidal direction in a simple way. Because of this, measurements of divertor parameters are required across the whole surface of the divertor plate in order to ensure an overlap between the projection from the upstream and the measurement area of diagnostics for the divertor. This complicates substantially the analysis, as it renders that probe systems on the target impractical for this analysis, as they are arranged in an array extending across the divertor along the poloidal direction [53] (figure 1 therein).

Given the need for a full 2D diagnostic, we resort to the infrared camera systems (IR) installed in W7-X [54]: this diagnostic captures thermographic images of the full divertor surface thus covering the projected area from the upstream measurements. Those images are used as an input for THEODOR code [55], which calculates the heat fluxes that reach the target

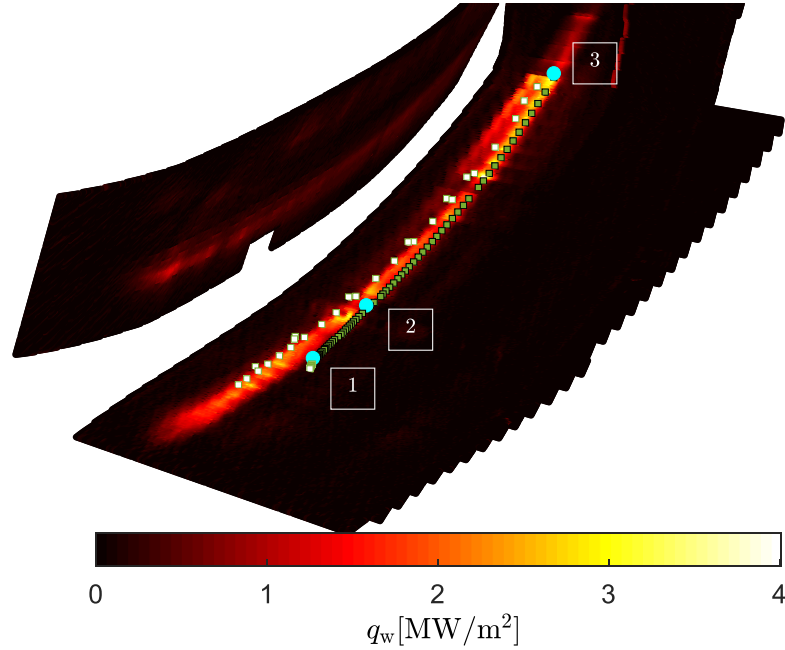


**Figure 4.** For program 20 180 905.017 ( $t = 4750\text{--}5000$  ms) the heat fluxes  $q_w$  onto the target s11h along with the projection of the measurement area with square markers.

wall ( $q_w$ ). Typically, IR data cannot be reliably used for this analysis if the ratio of  $P_{\text{rad}}/P_{\text{ECH}} > 0.5$ , where  $P_{\text{rad}}$  is the power radiated by the plasma, due to the low signal to noise ratio. This is limiting our study mainly to not detached plasmas. In figure 4, we show the heat flux onto target s11h for W7-X program 20 180 905.017 ( $t = 4750\text{--}5000$  ms) as an example. In figure 4, the projection of the measurement area is also included with square markers. We see that our projection from the SOL lies close to the strike point, around the region where the most intense heat fluxes are observed. It is now possible to extract the heat flux onto the divertor for its corresponding measurement point in the SOL, which is displayed in figure 5. For  $T_i \simeq T_e$  in the vicinity of the divertor, which is to be expected, considering that usually this condition is already met at the vicinity of the LCFS [56], ion reflection is considered negligible (which is typically the case for a carbon target) and the usual sheath entrance condition  $v_s = c_s$  is taken, the heat flux entering the sheath in front of the wall,  $q_t$  can be expressed in terms of the plasma parameters as in [57]:

$$q_t = c_s n_{c,s} [\gamma_s T_{e,s} + E_{\text{rec}}] \quad (4)$$

where  $c_s$  is the isothermal sound speed at the entrance of the sheath,  $c_s = \sqrt{2T_e/m_i}$  and  $\gamma_s \simeq 7.5$  is a sheath transmission coefficient.  $E_{\text{rec}}$  is the energy delivered to the target due to the atomic processes (including both ionization and dissociation energies), which can be considered constant and will therefore not matter for the discussion of this work [58]. Using the process previously described, it is possible to use the heat fluxes obtained from IR measurements to evaluate the decay of the heat flux over the DR measurement projection at the target and use it to provide an estimation of the temperature decay in order to evaluate the relation

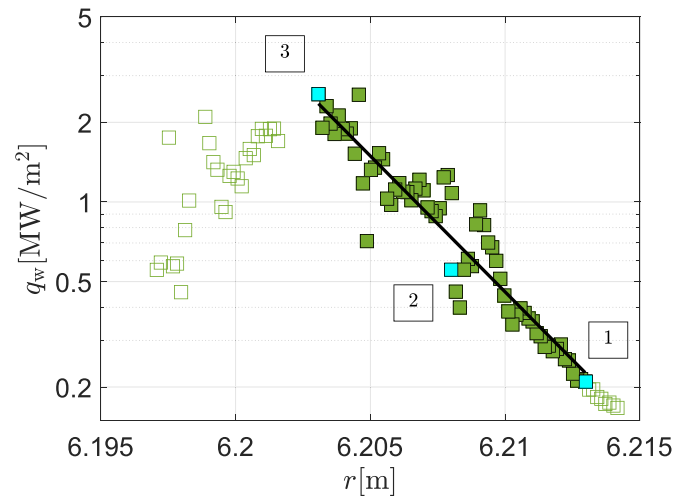


**Figure 5.** Heat fluxes for each point on the divertor from figure 4 for W7-X program 20 180 905.107 ( $t = 4750\text{--}5000$  ms). Hollow markers correspond to points that were not used for the fit and the calculation of  $\lambda_q$  through the linear fit (solid black line). The three cyan numbered markers correspond to the numbered markers of figure 3.

described in equation (3). In particular, if an exponential decay is assumed,  $q_t = q_0 \exp(-r/\lambda_q)$ , the exponential decay length at the entrance of the sheath,  $\lambda_q$  can be computed. If a similar exponential decay is assumed for the density, for weak parallel gradients in the SOL, the radial derivative of equation (4) becomes  $\lambda_q^{-1} = \lambda_n^{-1} + \frac{3}{2} \lambda_T^{-1}$ . By taking  $\lambda_n \simeq \lambda_T$  (which seems reasonable looking e.g. at the target profiles from [28]), this can be further simplified to  $\lambda_q \simeq \frac{2}{5} \lambda_T$ . In the conduction limited regime, featuring strong parallel gradients,



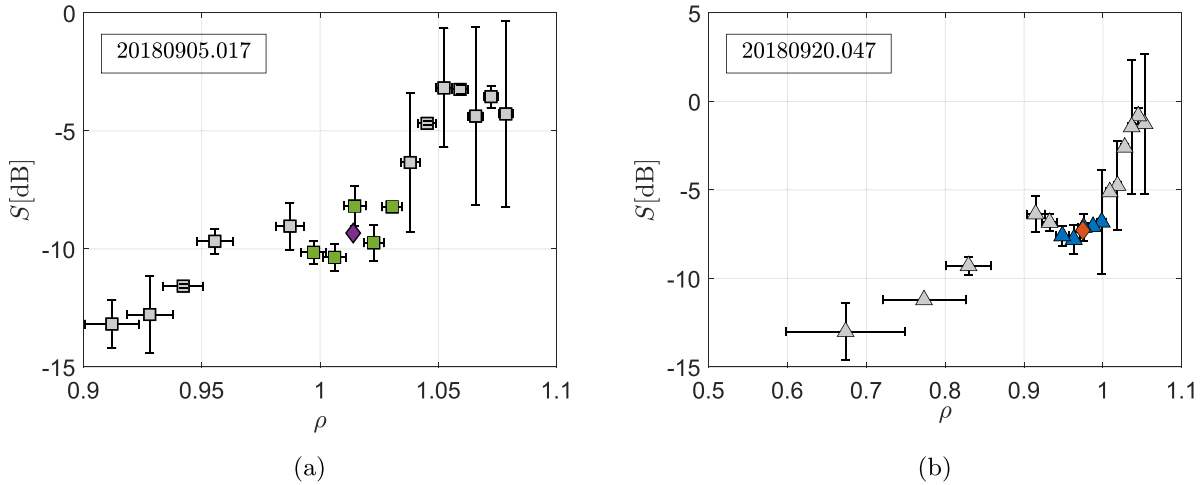


**Figure 6.**  $S$  profiles by the DR for discharge 20180905.017 ( $t = 4750$  ms to  $t = 5000$  ms) and for discharge 20180920.047 ( $t = 7000$  ms to  $t = 7250$  ms). The colored points, with green for 20180905.017 and blue for 20180920.047, were considered for the calculation of  $\bar{S}_{\min}$ , which is indicated with purple and orange diamond markers, respectively.

the two-point model relation  $\lambda_q \simeq \frac{2}{7} \lambda_T$  can be used instead [57]. This means that the two e-folding lengths are probably such that  $\frac{2}{7} < \lambda_q / \lambda_{Te} < \frac{2}{5}$ , and  $\lambda_q \propto \lambda_T$  in any of the two cases. It must be taken into account that these  $q_t$  and  $\lambda_q$  refer to the heat flux entering the sheath, while the IR system measures the heat flux perpendicular to the target wall,  $q_w$ . The two quantities differ due to the grazing angle ( $\alpha$ ) between the magnetic field lines and the divertor target plates  $q_w = q_t \sin(\alpha)$  [59]. However,  $\alpha$  is not found to change significantly at the relevant projection region of the divertor for the standard configuration, so it can be considered that  $q_w \propto q_t$  all across the region where  $\lambda_q$  is calculated. Thus,  $\lambda_q$  can be used as a qualitative proxy for the temperature decay length in equation (3).

In order to carry out the analysis, certain criteria must be established for the points that will be used for the calculation of the referred exponential decay length. The starting point for the fit should be considered the point with the maximum heat flux (see marker 3 on figure 5), including points for increasing values of  $r$ . The second criterion is related to the minimum meaningful value of  $q_w$ , below which points should not be considered. Points with  $q_w < 0.20 \text{ MW m}^{-2}$  are too close to the background noise level and excluded since the quality of the IR measurements is considered insufficient for them (see marker 1 and for increasing  $r$  the hollow markers on figure 5). As well, points that are too close to the LCFS should be excluded. In particular, it has been determined that points with  $r$  less than  $\sim 6.2$  m should be excluded from the fit since the total connection length ( $L$ ) increases very rapidly in a radial region of an extension below the spatial resolution of the FLT code. A representative example of this (corresponding to discharge 20180905.017) can be seen in figure 1(c), where  $L$  values diverge over 350 m for  $r < 6.2$  m. Since we cannot know whether those points are indeed outside or inside the LCFS, they are excluded from the linear fit and depicted as hollow markers on the left of figure 5. Finally, those remaining points that are eligible for the fit are shown as markers filled with

green color. The electron temperature for the ratio on the rhs of equation (3) is calculated through the TS temperature profiles at the LCFS since low parallel gradients are assumed from the LCFS to the sheath entrance.

#### 2.4. Density fluctuation profiles

As mentioned in section 1, the other main objective of this work is to seek any trends between  $\Delta E_r$  (as defined in figure 2) and the amplitude of edge turbulence. For this task, we used the density fluctuation measurements from the DR. In figures 6(a) and (b), the  $S \propto \delta n_e^2$  profiles are shown for values around  $\rho = 1$ . For both discharges, approximately at the same position as the  $E_r$  sign reversal, a local minimum of the power collected by the DR is observed for a number of measurement points, as indicated by the colored markers in figures 6(a) and (b). By taking the average value of  $S$  and  $\rho$  of points that constitute this local minimum, it is possible to define the average reduced level of power collected by the DR ( $\bar{S}_{\min}$ , as the diamond marker with distinct color on each figure). For example, in the previously discussed cases 20180905.017 and 20180920.047,  $\bar{S}_{\min}$  is found approximately  $-9.3$  dB and  $-7.3$  dB respectively, with an uncertainty of the order of 2 dB. This approach will be used in section 3 for a bigger list of experiments, in or between  $\Delta E_r$  and  $\bar{S}_{\min}$ .

### 3. Results

For the purposes of this study, a set of various plasmas heated with ECH was analyzed. The standard configuration was preferred over other configurations due to the fact that it was used most commonly during OP1.2. In the selected discharges, that are presented in a parametric map on figure 7, we have explored the available range of density and heating powers that could guarantee the existence of measurement points of the DR in the SOL. For each point of this figure a full DR

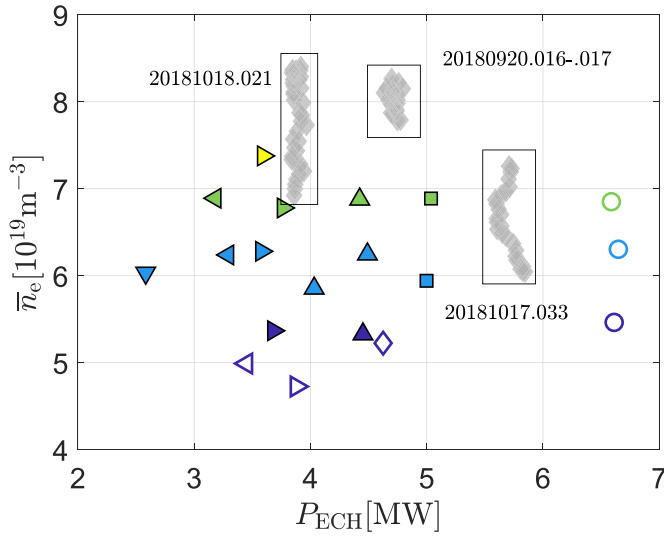


**Figure 7.** Parametric map with all analyzed discharges displayed as a function of the ECH power ( $P_{\text{ECH}}$ ) and line averaged density ( $\bar{n}_e$ ) that are considered in this work. Gray markers and hollow markers depict discharges that will be used for the study of the edge  $E_r$  shear and turbulence reduction but not for the study on the formation of the  $E_{r,\text{SOL}}$ .

frequency scan was analyzed for the indicated times. Colors on this plot indicate different levels of the line averaged electron plasma density,  $\bar{n}_e$ . Instead, different markers indicate similar values of ECH power. It can be seen that the range of line averaged densities varies from  $4.5 \times 10^{19} \text{ m}^{-3}$  to  $7.5 \times 10^{19} \text{ m}^{-3}$  which covers the plasma scenarios for which V-band frequencies with O-mode polarization can measure in the SOL region. The level of ECH power varies from 2.5 MW and 6.5 MW, the latter value being close to the maximum heating power coupled to the plasma in W7-X [29, 60]. For the formation of  $E_{r,\text{SOL}}$ , we studied plasmas with density from  $\simeq 5.5 \times 10^{19} \text{ m}^{-3}$  to  $7.5 \times 10^{19} \text{ m}^{-3}$  and ECH power from 2.5 MW to 5 MW. In table 1, we list the analyzed discharges along with the DR scan time intervals, the control coil currents and net toroidal plasma currents that we used as input for the FLT calculation. Hollow markers represent discharges for which the heat fluxes on the target are not available. Nevertheless, they are still included in our database since they will be used for the study of  $E_{r,\text{SOL}}$  by other plasma parameters (i.e.  $P_{\text{ECH}}$  or  $\bar{n}_e$ ) and the study for  $\Delta E_r$  and the reduced  $S$ . Discharges with gray markers concern also the  $\Delta E_r$  and the reduced  $S$  that will be discussed later.

### 3.1. Impact of the divertor on SOL radial electric field

First, we study the evolution of  $\bar{E}_{r,\text{SOL}}$  (calculated as explained in section 2) with respect to basic plasma parameters, like  $\bar{n}_e$  and  $P_{\text{ECH}}$ . In figures 8(a) and (b),  $\bar{E}_{r,\text{SOL}}$  is plotted against the  $\bar{n}_e$  and  $P_{\text{ECH}}$  respectively. In figure 8(a), for increasing line averaged density and constant ECH power (see markers of similar shape but different color), the value of the radial electric field in the SOL region is decreasing. In figure 8(b), for increasing ECH power and constant density (see markers

**Table 1.** Showing discharge numbers, the DR scan time intervals,  $I_{\text{CC}}$  and  $I_{\text{tor}}$  of the ECH plasmas used for the given analysis. Additionally, the equivalent marker of each DR scan for figure 7 is given in the last column. All discharges employ the standard configuration of W7-X. When  $I_{\text{tor}} \ll 1 \text{ kA}$ , its value was considered negligible.

Discharge number	DR scan times (ms)	$I_{\text{CC}}$ (kA)	$I_{\text{tor}}$ (kA)	Marker
20 180 807.022	4000–4252	0	1.84	◀
20 180 814.042	1000–1252	0	$\ll 1$	▶
20 181 010.012	2750–3001	0	1.93	◇
20 180 807.022	1250–1502	0	$\ll 1$	▶
20 181 010.012	1000–1252	0	$\ll 1$	▲
20 180 906.008	2000–2251	1	2.53	○
20 180 807.017	2000–2252	0	$\ll 1$	▼
20 180 814.010	1000–1252	2	$\ll 1$	◀
20 180 807.020	5500–5752	0	$\ll 1$	▶
20 180 920.047	7000–7252	0	2.51	▲
20 181 010.007	8500–8752	0	3.89	▲
20 180 905.016	1250–1502	2	1.25	■
20 180 906.008	4250–4502	1	4.38	○
20 180 905.015	10 500–10 753	0	1.71	◀
20 180 814.011	4500–4751	0	$\ll 1$	▶
20 181 010.019	5750–6001	0	2.70	▲
20 180 905.017	4750–5002	1	3.21	■
20 180 906.008	6250–6501	1	5.58	○
20 180 807.020	1250–1502	0	$\ll 1$	▶

of similar color but different shape), the radial electric field in the SOL is increasing. This result is consistent with previous reports [18], covering a shorter range of ECH power values. From figures 8(a) and (b), it could be assumed that there is a proportional relationship of  $\bar{E}_{r,\text{SOL}}$  to ECH power and inversely proportional to the line density. This is confirmed in figure 8(c) where  $\bar{E}_{r,\text{SOL}}$  is plotted against the ratio of  $P_{\text{ECH}}/\bar{n}_e$ . As can be seen, a rather linear relation exists between both parameters for the whole set of data, suggesting  $\bar{E}_{r,\text{SOL}} \propto P_{\text{ECH}}/\bar{n}_e$ . The scattering of the points in figure 8(c) is reduced with respect to the scattering of the points in figures 8(a) and (b). Thus, this ratio seems to set a much clearer linear trend in the value of the mid-plane electric field than solely  $\bar{n}_e$  or  $P_{\text{ECH}}$ .

Next, we evaluate the influence of the downstream divertor conditions on the mid-plane radial electric field. In figure 9, we plot  $\bar{E}_{r,\text{SOL}}$  and the ratio of the electron temperature over the exponential decay length of the heat flux,  $T_e/\lambda_q$ . The plotted data shows that  $\bar{E}_{r,\text{SOL}}$  scales clearly with the ratio  $T_e/\lambda_q$ , roughly verifying for the whole database the relation described in equation (3). Despite the approximations discussed in the previous sections, the radial electric field in the SOL appears to be dominated by the conditions on the divertor for the studied plasmas. The uncertainty bars of the radial electric field are computed as the standard deviation of the points that we used to compute the mean average value. The uncertainty bars of  $\lambda_q$  were calculated from linear regression on the points of figure 5. For the majority of discharges, the relevant divertor target was s1lh. However, for discharges 20 181 010.007 and 20 181 010.019 (both of them featuring high toroidal plasma

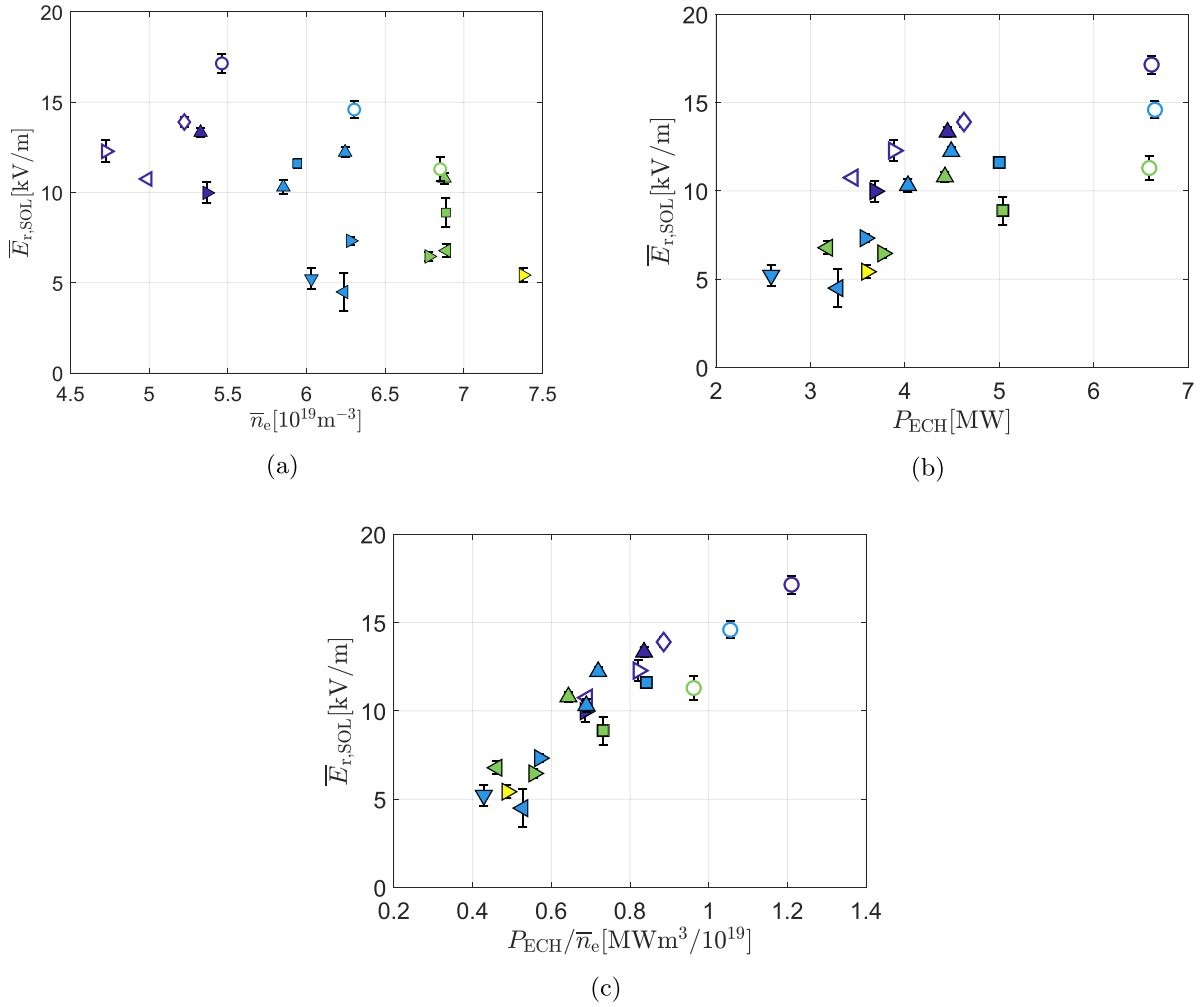


**Figure 8.**  $\bar{E}_{r,SOL}$  as a function of  $\bar{n}_e$  (a),  $P_{ECH}$  (b) and the  $P_{ECH}/\bar{n}_e$  ratio (c). The use of markers and colors is the same as in figure 7.

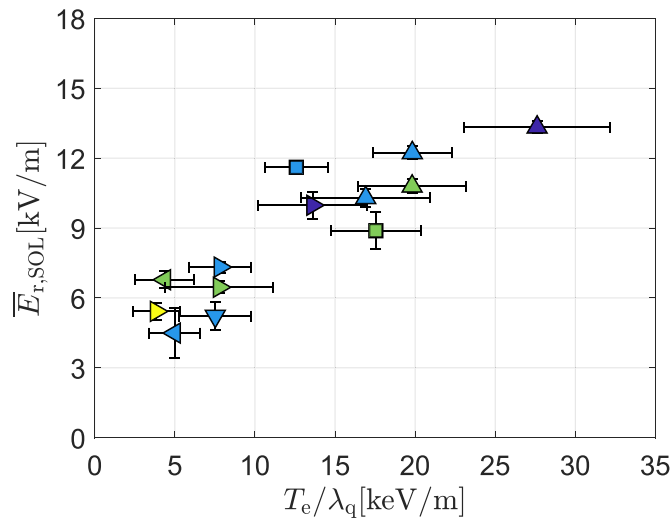


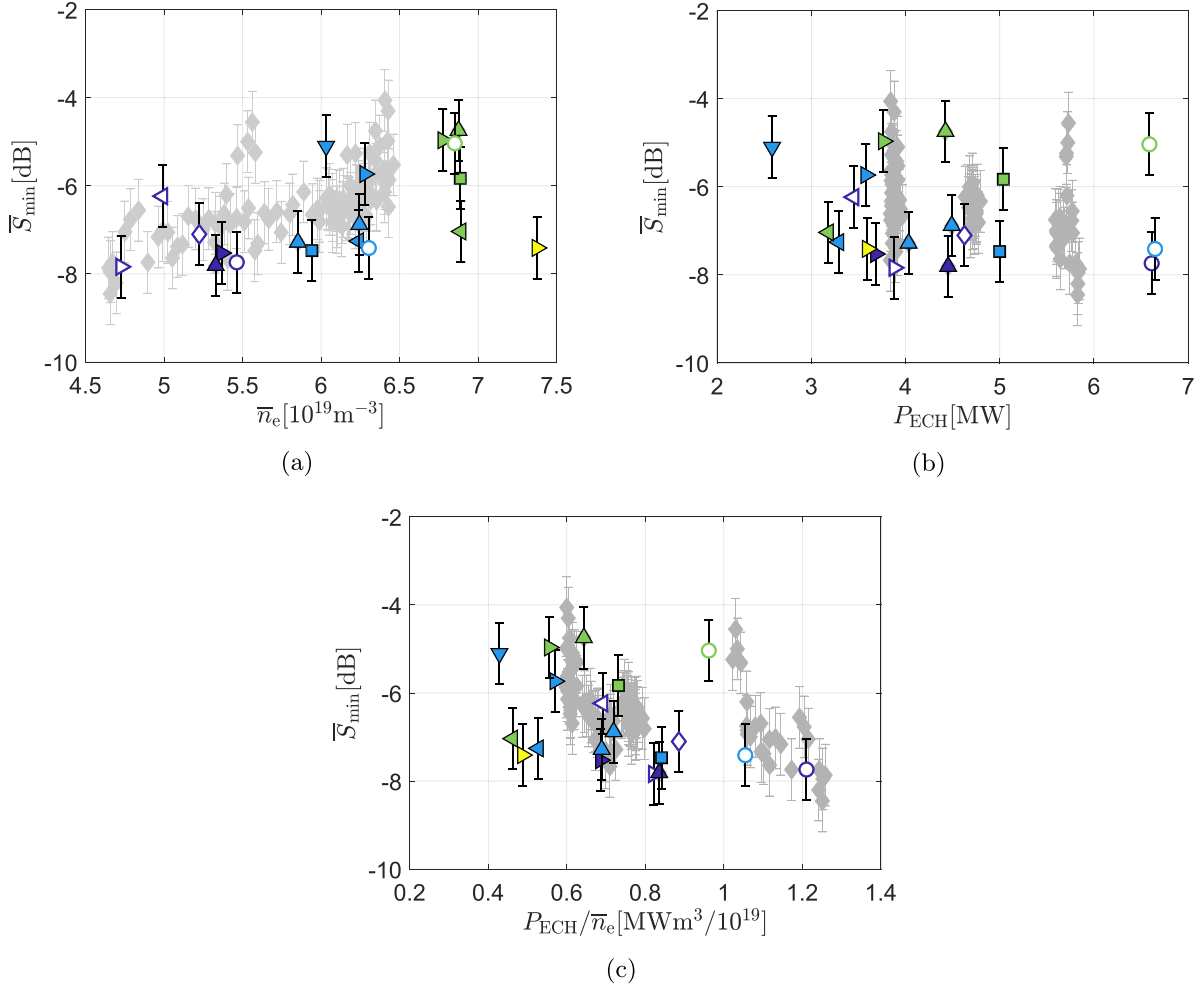
**Figure 9.**  $\bar{E}_{r,SOL}$  and the ratio of the electron temperature with the exponential decay length of heat fluxes at the target,  $T_e/\lambda_q$ . The use of markers and colors is the same as in figure 7.

currents, 3.9kA and 2.7kA respectively with no current in the control coils), the FLT analysis showed that the region relevant for the calculation of  $\lambda_q$  was found at the s4uv target. A

mapping of different positions in the island onto the different divertor targets of W7-X has been shown in [37]. Nevertheless, both groups of points seem to merge seamlessly in figure 9,

**Table 2.** Table with discharge numbers, the given DR scans,  $\bar{n}_e$  and  $P_{\text{ECH}}$  of the ECH plasmas used for the given analysis. All discharges employ the standard configuration of W7-X.

Discharge number	DR scan times (ms)	$\bar{n}_e$ ( $10^{19} \text{ m}^{-3}$ )	$P_{\text{ECH}}$ (MW)
20 180 920.016	2250–6000	6.2	4.5
20 180 920.017	2000–6000	6.2	4.5
20 181 017.033	2750–9500	4.6–5.8	<6
20 181 018.021	1000–12 000	5.4–6.5	4

**Figure 10.** The back-scattered power  $S \propto \delta n_c^2$  as a function of  $\bar{n}_e$  (a),  $P_{\text{ECH}}$  (b) and the  $P_{\text{ECH}}/\bar{n}_e$  ratio (c). The use of markers and colors is the same as that was given in figure 7.

indicating that the changes on the SOL magnetic field structure induced by the toroidal current do not significantly affect the general trend.

### 3.2. Effect of $E_r$ shear on the edge fluctuation level

Since only DR data is required for the study of the impact of  $\Delta E_r$  on edge turbulence, it was possible to expand the existing database including other discharges with numerous scans of the reflectometer (96 additional DR scans from 4 more discharges). In table 2 we present the discharge numbers with the corresponding time intervals of the extra DR scans. As well, in figure 7, these discharges are represented as gray points, to set

them apart from the ones on which IR data is discussed. Interestingly, two of them (20 181 017.033 and 20 181 018.021) feature density ramps, on which  $\bar{n}_e$  is steadily increased while keeping constant the ECH power. Further details on these data can be found elsewhere in the literature [61].

As with  $\bar{E}_{r,\text{SOL}}$ , we first study the evolution of  $\bar{S}_{\text{min}}$ , calculated as explained in section 2, with respect to basic plasma parameters,  $\bar{n}_e$ ,  $P_{\text{ECH}}$  and the ratio of the two quantities,  $P_{\text{ECH}}/\bar{n}_e$ . As can be seen in figure 10, there is no apparent trend between the  $\bar{S}_{\text{min}}$  and ECH power (figure 10(b)) nor between  $\bar{S}_{\text{min}}$  and the  $P_{\text{ECH}}/\bar{n}_e$  ratio (figure 10(c)). In figure 7, the DR scans included in table 2 are depicted with gray markers while the DR scans included in table 1 using the same marker and

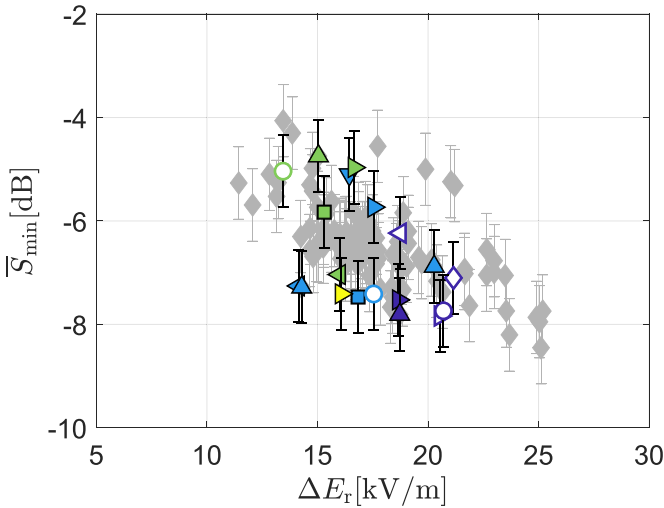


**Figure 11.**  $\bar{S}_{\min}$  against  $\Delta E_r$  for the DR scans given in tables 1 and 2. The gray markers represent the extra DR scans that have been introduced in this study while the DR scans of the previous study are represented by the same markers as in figure 7.

color as in the figure above. In figure 10(a), some relation can be seen between  $\bar{S}_{\min}$  and line averaged density, with an increment of about 5 dB over the observed density range (from  $-9$  dB to  $-4$  dB for an increment of the line averaged density from  $4.5$  to  $6.5 \times 10^{19} \text{ m}^{-3}$ ). This is particularly clear for the density ramps featured in the gray data. Finally, in figure 11,  $\bar{S}_{\min}$  is plotted against difference of the radial electric field at the sign reversal for the DR scans,  $\Delta E_r$ , which is considered a proxy for the velocity shear at the edge. In it, an inverse relation between the two parameters is observed, arguably clearer than any of the ones seen in figure 10, indicating that there is some degree of turbulence suppression when the radial electric field shear becomes stronger. As well, the scattering of the points in the plot is found to decrease for increasing  $\Delta E_r$ . However, it must be pointed out that this decrease is rather moderate: since  $S \propto \delta n_e^2$ , the 5 dB decay observed over the whole range of shear values represents a reduction of less than a factor 2 in the density fluctuation amplitude. Interestingly, this factor is rather close to the ratio between the highest and lowest line averaged densities in the database. This would indicate that, if the relative amplitude of the fluctuations  $\delta n_e/n_e$  does not change, the observed effect could be largely explained by the increase of density at the measurement points at the edge of the plasma (which roughly follows that of  $\bar{n}_e$ ).

#### 4. Discussion and summary

The first objective of this work was to investigate the mechanism behind the formation of the electric field at the SOL of a stellarator with an island divertor. By analyzing divertor conditions over a set of standard configuration plasmas featuring a wide range of  $\bar{E}_{r,\text{SOL}}$  values in attached divertor conditions ( $P_{\text{rad}}/P_{\text{ECH}} < 0.5$ ), we have determined that the radial electric field at the SOL of the elliptic section follows the  $\bar{E}_{r,\text{SOL}} \propto T_e/\lambda_q$  relation expressed in equation (3). If some

reasonable assumptions are made (namely,  $\lambda_q \propto \lambda_T$  and small variation of the incidence angle of the magnetic field at the target over the projection of the upstream measurement region, leading to  $q_t \propto q_w$ ), this can be interpreted as a proof that parallel current and gradients of electron temperature and pressure are small and the upstream potential is determined by the sheath entrance potential under these conditions,  $\phi_u \simeq \phi_s$ . Since  $\phi_s \simeq 3T_e$ , this means that the potential profile in the SOL of W7-X in attached conditions is determined by the  $T_e$  values at the divertor. This simple tokamak model is consistent with modeling carried out in the predecessor machine W7-AS [26] and with previous observations at W7-X, which indicated that the main SOL drift for low density plasmas was caused by the radial electric field,  $E_r \times B$  [28]. In the later case, the poloidal drifts caused by the  $E_r$  at the SOL are dominant for low density but are substantially decreased for the high density case. This is consistent with the reduction of  $E_{r,\text{SOL}}$  in figure 8(a). More recent studies [62, 63] have investigated the impact of drifts on parallel flows, as observed by coherence spectroscopy. Their results point towards a rather similar picture: for low density plasmas, strong poloidal drifts cause a strong deviation of the parallel stagnation points with respect to the X point, where they would be expected if the effect of drifts is not taken into account (as is the case of EMC3-EIRENE simulations discussed in those works). Instead, when density is increased, the effect of the  $E_r \times B$  drift decreases, resulting in reduced asymmetries and the development of a counter-streaming flow pattern. Interestingly, all these results are best understood once evidence on the link between divertor conditions and the mid-plane  $E_r$  value has been provided, as they fit well in the classical physical picture for the formation of the electric field discussed in the introduction, according to which the increase in density flattens  $T_e$  gradients at the target, while increasing collisionality and parallel gradients and thus raising a substantial  $E_{\parallel}$ . Therefore, our results imply that the intensity of the SOL drifts for attached plasmas would be dominated by the steepness of the  $T_e$  profile at the target.

A few more remarks concerning the results on the formation of  $E_{r,\text{SOL}}$  are in order: first, it must be taken into account that the DR used in this work can only measure at one position in the SOL of W7-X (corresponding to the bean-shaped plasma section shown in figure 1). Given the complex, non-axisymmetric topology of the island divertor, it cannot be assumed that this will be automatically the case for any other position and the determination of  $\phi_u$  will be considerably more complicated for regions which are not directly connected to the targets. In order to obtain a full physical picture of the formation of the radial electric field, this study should be extended to plasmas with  $P_{\text{rad}}/P_{\text{EC}} > 0.5$  (this is, with a lower  $P_{\text{ECH}}/\bar{n}_e$  ratio) featuring different degrees of detachment. If the relation to the proposed basic model holds, the link between  $\bar{E}_{r,\text{SOL}}$  and target conditions should disappear, and other factors (such as the local parallel currents) should become dominant. This kind of investigation cannot be carried out using the approach presented in the present study (and thus falls out of its scope), as the IR data can no longer be relied for it, and therefore the simple estimation of  $\lambda_q$  used here is no longer possible. Instead, a complex combination of different diagnostics



(such as Langmuir fixed probes at the targets, mid-plane manipulator, Helium beam, etc) and simulations will be required to identify the SOL conditions which follow the variation of  $\bar{E}_{r,SOL}$  as measured by the DR in this higher density regime. Finally, this work only deals with plasmas in the standard configuration. Changing the configuration may as well have important implications on the formation of the  $E_r$  at the SOL. So far, we can expect the region of the plasma-wall interaction to change. As a result, the projection of the DR measurement area to the divertor will change with respect to that of the standard configuration and therefore  $\lambda_q$  would need to be fitted elsewhere on the target. More importantly, changes in the magnetic field configuration lead to different iota profiles. This is relevant, as configurations with higher values of iota, have reduced connection lengths and thus reduced width of the SOL [64]. As a result, perpendicular transport should be also reduced in them, resulting in a lower value of  $\lambda_q$  at the target and according to the mechanism discussed in this work, should feature higher values of  $E_{r,SOL}$  caused by the enhanced  $T_e$  gradients at the target. Available measurements of  $E_{r,SOL}$  in different configurations are thus consistent with our results: high iota features higher radial electric fields in the SOL than the standard configuration for a given set of density and heating power [18]. The effect of magnetic configuration on  $E_{r,SOL}$  formation must also be clarified before a quantitative comparison of our results can be carried out with drift experiments previously discussed, as they are typically carried out in low iota configuration. However, the qualitative trend relating connection length and  $T_e$  gradients at the target is also consistent in those studies: the density over which the counter-streaming flows abruptly appear (indicating the reduction of the  $E_r$ -induced stagnation point shift) is around  $3 \times 10^{19} \text{ m}^{-3}$  [63], substantially lower than the values over which the  $E_{r,SOL}$  is reduced in the present work. This could be similarly explained by the longer connection lengths found in the low iota configuration when compared to the standard, which would lead to increased SOL width and lower values of  $n_e$  and  $P_{ECH}$  for a given value of  $E_{r,SOL}$  (as is the case between high iota and standard configuration in [18]). These effects will be addressed in forthcoming experimental campaigns by extending the standard configuration database including equivalent scenarios in magnetic configurations with different iota profiles.

The second objective of this study was to determine whether the observed variations on the amplitude of the velocity shear observed across the LCFS have the expected suppression effect on the local turbulence. In this case, we combined measurements of the radial electric field and fluctuation amplitude profiles, both carried out by the DR. By doing so, we find that there is typically a depression of several dB in the profile of fluctuation amplitude which roughly coincides with the position of the change of sign of the radial electric field (where the shear would be at its maximum). This effect, which was shown for typical discharges in figure 6, is indicative of the shear suppression mechanism. Then, we try to quantify the effect of the shear by comparing discharges with different density and heating power. As seen in figure 11, we observe that fluctuation amplitude at the shear region do

indeed decrease as the radial electric field jump between the SOL and the confined region becomes larger. However, this reduction in amplitude is rather moderate (the 5 dB observed in the figure correspond to a variation of around 80% in  $\delta n$ ) and just marginally above the uncertainty bars of the measurements. Moreover, given the already discussed evolution of the SOL electric field with plasma parameters,  $E_{r,SOL}$ , and consequently  $\Delta E_r$ , are reduced for discharges with higher density. Therefore, at least part of the apparent suppression of fluctuations can be simply explained by the reduction of local density at the measurement point (and indeed, fluctuation amplitude shows as well some correlation to line averaged density, as seen in figure 10). This result suggests that the effect on fluctuations of the velocity shear observed around the LCFS of W7-X is rather moderate, which is against expectations from studies at tokamaks, specially considering the non-negligible values of  $\Delta E_r$ , which reach up to  $25 \text{ kV m}^{-1}$ . In any case, the fact that fluctuation amplitude is clearly decreasing around the edge  $E_r$  shear for a given discharge (as seen for example in figure 6), indicates that at least some degree of shear-related suppression is most likely taking place. Considering all of the above, it is difficult to achieve a strong conclusion here: indeed,  $\Delta E_r$  is only a proxy for the shear which does not take into account the steepness of the  $E_r$  profile. The reason for this is the poor quality of density profiles at the edge of W7-X, which did not permit an accurate enough localization of the DR measurements in previous campaigns. This may be expected to improve in forthcoming campaigns thanks to upgrades on the TS system and the routine availability of alkali beam data [65]. While  $\Delta E_r$  allows for a qualitative discussion of the shear intensity (e.g. between different discharges), it does not suffice for a comparison on the shearing rate with the autocorrelation time of the observed amplitude. As a consequence, it is difficult to know if the  $k_{\perp}$  range of fluctuations observed by the DR in these discharges is below or above the spatial scale which should be decorrelated by the shear. As well, other examples exist of instances in which a strong radial gradient of  $E_r$  seems to be followed by a strong local reduction of the fluctuation amplitude, as measured by the DR. One such case is the strong sheared structure caused in  $u_{\perp}$  when an island chain of sufficient width is found inside the LCFS [45]. Therefore, while no clear evidence of shear-suppression effect on the turbulence has been found in this work, this analysis will need to be refined before it can be safely stated that there is no such mechanism at W7-X. In future experiments, upgrades for the DR system [66] will be available in order to carry out a more detailed characterization of turbulence in the region, including wave number spectra and correlation studies which may shed light onto the effect of the shear on the elongation of eddies. Finally, beyond the specific effect of the shear on density fluctuations, its impact on turbulent transport should be systematically evaluated in order to determine its impact the overall performance of W7-X and thus assess the relevance of this phenomenon.








In summary, this study shows for the first time that the physics behind the formation of the electric field at the SOL of an island-divertor stellarator is qualitatively the same as in a tokamak, at least when the divertor is attached. This means that

the radial electric field, which is responsible for the main SOL drifts in this regime, depends on the  $T_e$  values at the entrance of the sheath. The variation of the radial electric field around the separatrix of W7-X leads to a local reduction of the amplitude of density fluctuations, as expected from both models and experiments carried out in tokamaks. However, when different amplitudes of such shear-linked to the correspondingly different divertor conditions are compared, a rather moderate effect on the fluctuations is observed. While this result initially hints that the edge shear could be a less efficient mechanism for the formation of edge transport barriers as it is in tokamaks, a more complete investigation is required before solid conclusions can be reached. This will be carried out in the forthcoming experimental campaigns of Wendelstein 7-X.

## Acknowledgments

The authors acknowledge the entire W7-X team for their support. This work has been partially funded by the Spanish Ministry of Science and Innovation under Contract No. FIS2017-88892-P and PID2021-125607NB-I00. This work has been sponsored in part by the Comunidad de Madrid under Project 2017-T1/AMB-5625. This work has been carried out within the framework of the EUROfusion Consortium, funded by the European Union via the Euratom Research and Training Programme (Grant Agreement No. 101052200—EUROfusion). Views and opinions expressed are however those of the author(s) only and do not necessarily reflect those of the European Union or the European Commission. Neither the European Union nor the European Commission can be held responsible for them.

## ORCID iDs

E. Maragkoudakis  <https://orcid.org/0000-0001-7329-4001>  
 D. Carralero  <https://orcid.org/0000-0002-7824-3307>  
 T. Estrada  <https://orcid.org/0000-0001-6205-2656>  
 Y. Gao  <https://orcid.org/0000-0001-8576-0970>  
 C. Killer  <https://orcid.org/0000-0001-7747-3066>  
 M. Jakubowski  <https://orcid.org/0000-0002-6557-3497>  
 M. Vecsei  <https://orcid.org/0000-0003-4596-1211>  
 S. Zoletnik  <https://orcid.org/0000-0002-7324-2647>  
 A. Cappa  <https://orcid.org/0000-0002-2250-9209>

## References

- [1] Goldston R. 2011 Heuristic drift-based model of the power scrape-off width in low-gas-puff H-mode tokamaks *Nucl. Fusion* **52** 013009
- [2] Rozhansky V., Molchanov P., Veselova I., Voskoboinikov S., Kirk A. and Coster D. 2012 Contribution of drifts and parallel currents to divertor asymmetries *Nucl. Fusion* **52** 103017
- [3] Grieger G., Beidler C., Harmeyer E., Lotz W., Käßlinger J., Merkel P., Nührenberg J., Rau F., Strumberger E. and Wobig H. 1992 Modular stellarator reactors and plans for Wendelstein 7-X *Fusion Technol.* **21** 1767–78
- [4] Bosch H.S. *et al* 2013 Technical challenges in the construction of the steady-state stellarator Wendelstein 7-X *Nucl. Fusion* **53** 126001
- [5] Klinger T. *et al* 2017 Performance and properties of the first plasmas of Wendelstein 7-X *Plasma Phys. Control. Fusion* **59** 014018
- [6] Pedersen T.S. *et al* 2022 Experimental confirmation of efficient island divertor operation and successful neoclassical transport optimization in Wendelstein 7-X *Nucl. Fusion* **62** 042022
- [7] Biglari H., Diamond P.H. and Terry P.W. 1990 Influence of sheared poloidal rotation on edge turbulence *Phys. Fluids B* **2** 1–4
- [8] Taylor R.J., Brown M.L., Fried B.D., Grote H., Liberati J.R., Morales G.J., Pribyl P., Darrow D. and Ono M. 1989 H-mode behavior induced by cross-field currents in a tokamak *Phys. Rev. Lett.* **63** 2365–8
- [9] Moyer R.A., Tynan G.R., Holland C. and Burin M.J. 2001 Increased nonlinear coupling between turbulence and low-frequency fluctuations at the  $l-h$  transition *Phys. Rev. Lett.* **87** 135001
- [10] Viezzer E., Pütterich T., Angioni C., Bergmann A., Dux R., Fable E., McDermott R., Stroth U. and Wolfrum E. (The ASDEX Upgrade Team) 2013 Evidence for the neoclassical nature of the radial electric field in the edge transport barrier of ASDEX upgrade *Nucl. Fusion* **54** 012003
- [11] Brakel R. *et al* 1997 Confinement in W7-AS and the role of radial electric field and magnetic shear *Plasma Phys. Control. Fusion* **39** B273–86
- [12] Happel T., Estrada T. and Blanco E. 2011 Scale-selective turbulence reduction in H-mode plasmas in the TJ-II stellarator *Phys. Plasmas* **18** 102302
- [13] Andrew Y. *et al* (JET-EFDA Contributors) 2008 Evolution of the radial electric field in a JET H-mode plasma *Europhys. Lett.* **83** 15003
- [14] Estrada T. *et al* 2009 Sheared flows and transition to improved confinement regime in the TJ-II stellarator *Plasma Phys. Control. Fusion* **51** 124015
- [15] LaBombard B. *et al* 2005 Transport-driven scrape-off layer flows and the  $x$ -point dependence of the  $L-H$  power threshold in Alcator C-Mod *Phys. Plasmas* **12** 056111
- [16] Chankin A.V., Corrigan G. and Maggi C.F. 2019 EDGE2D-EIRENE simulations of the influence of isotope effects and anomalous transport coefficients on near scrape-off layer radial electric field *Plasma Phys. Control. Fusion* **61** 075010
- [17] Krämer-Flecken A. *et al* 2020 Investigation of turbulence rotation in the SOL and plasma edge of W7-X for different magnetic configurations *Plasma Sci. Technol.* **22** 064004
- [18] Carralero D. *et al* 2020 Characterization of the radial electric field and edge velocity shear in Wendelstein 7-X *Nucl. Fusion* **60** 106019
- [19] Stangeby P. and Chankin A. 1996 Simple models for the radial and poloidal  $E \times B$  drifts in the scrape-off layer of a divertor tokamak: effects on in/out asymmetries *Nucl. Fusion* **36** 839–52
- [20] Jaervinen A.E. *et al* 2018  $E \times B$  flux driven detachment bifurcation in the DIII-D tokamak *Phys. Rev. Lett.* **121** 075001
- [21] Silva C. *et al* (JET Contributors) 2021 Structure of the JET edge radial electric field in He and D plasmas *Nucl. Fusion* **61** 126006
- [22] Brida D., Conway G., Adamek J., Silvagni D., David P., Eich T., Grenfell G., Komm M. and Plank U. 2022 Physics of the electric field in the scrape-off layer in ASDEX Upgrade L-mode discharges and comparison to experiments *Nucl. Mater. Energy* **33** 101262

- [23] Wensing M. *et al* 2020 Experimental verification of X-point potential well formation in unfavorable magnetic field direction *Nucl. Mater. Energy* **25** 100839
- [24] Grigull P. *et al* 2003 Influence of magnetic field configurations on divertor plasma parameters in the W7-AS stellarator *J. Nucl. Mater.* **313–316** 1287–91
- [25] Feng Y., Sardei F., Grigull P., McCormick K., Giannone L., Kisslinger J., Reiter D., Igitkhanov Y. and Wenzel U. 2003 Modelling of island divertor physics and comparison to W7-AS experimental results *J. Nucl. Mater.* **313–316** 857–62
- [26] Feng Y., Sardei F., Grigull P. and Herre G. 1999 Drift effects in W7-AS limiter and island divertor configurations *J. Nucl. Mater.* **266** 928–33
- [27] Feng Y., Sardei F. and Kisslinger J. 1999 3D fluid modelling of the edge plasma by means of a Monte Carlo technique *J. Nucl. Mater.* **266** 812–18
- [28] Hammond K.C. *et al* 2019 Drift effects on W7-X divertor heat and particle fluxes *Plasma Phys. Control. Fusion* **61** 125001
- [29] Erckmann V. *et al* (W7-X ECRH Team at IPP Greifswald, W7-X ECRH Team at FZK Karlsruhe and W7-X ECRH Team at IPF Stuttgart) 2017 Electron cyclotron heating for W7-X: physics and technology *Fusion Sci. Technol.* **52** 291–312
- [30] Geiger J., Beidler C.D., Feng Y., Maaßberg H., Marushchenko N.B. and Turkin Y. 2014 Physics in the magnetic configuration space of W7-X *Plasma Phys. Control. Fusion* **57** 014004
- [31] Renner H., Boscaro J., Greuner H., Grote H., Hoffmann F.W., Kisslinger J., Strumberger E. and Mendelevitch B. 2002 Divertor concept for the W7-X stellarator and mode of operation *Plasma Phys. Control. Fusion* **44** 1005
- [32] Klinger T. *et al* 2019 Overview of first Wendelstein 7-X high-performance operation *Nucl. Fusion* **59** 112004
- [33] Feng Y., Sardei F., Grigull P., McCormick K., Kisslinger J. and Reiter D. 2006 Physics of island divertors as highlighted by the example of W7-AS *Nucl. Fusion* **46** 807
- [34] Feng Y. *et al* (W7-X Team) 2021 Understanding detachment of the W7-X island divertor *Nucl. Fusion* **61** 086012
- [35] Pedersen T.S. *et al* 2018 First results from divertor operation in Wendelstein 7-X *Plasma Phys. Control. Fusion* **61** 014035
- [36] Bozhenkov S.A., Geiger J., Grahl M., Kißlinger J., Werner A. and Wolf R.C. 2013 Service oriented architecture for scientific analysis at W7-X. An example of a field line tracer *Fusion Eng. Des.* **88** 2997–3006
- [37] Killer C., Grulke O., Drews P., Gao Y., Jakubowski M., Knieps A., Nicolai D., Niemann H., Sitjes A.P. and Satheeswaran G. 2019 Characterization of the W7-X scrape-off layer using reciprocating probes *Nucl. Fusion* **59** 086013
- [38] Windisch T. *et al* 2015 Reflectometry fluctuation diagnostics at Wendelstein 7-X *42nd EPS Conf. on Plasma Physics (Lisbon, Portugal, 22nd–26th June 2015)* (available at: [www.ipfn.tecnico.ulisboa.pt/EPS2015/index.html](http://www.ipfn.tecnico.ulisboa.pt/EPS2015/index.html))
- [39] Windisch T. *et al* 2019 W-band Doppler reflectometry at Wendelstein 7-X: diagnostic setup and initial results *14th Int. Reflectometry Workshop (Lausanne, Switzerland, 22nd–24th May 2019)* (available at: [www.epfl.ch/research/domains/swiss-plasma-center/links/irw14/](http://www.epfl.ch/research/domains/swiss-plasma-center/links/irw14/))
- [40] Hirsch M., Holzhauser E., Baldzuhn J., Kurzan B. and Scott B. 2001 Doppler reflectometry for the investigation of propagating density perturbations *Plasma Phys. Control. Fusion* **43** 1641
- [41] Conway G.D., Schirmer J., Klengel S., Suttrop W. and Holzhauser E. 2004 Plasma rotation profile measurements using Doppler reflectometry *Plasma Phys. Control. Fusion* **46** 951
- [42] Manz P., Prisiazhniuk D., Happel T., Freethy S., Hallatschek K., Scott B.D. and Stroth U. 2018 On the phase velocity in between weak and strong plasma edge turbulence *Plasma Phys. Control. Fusion* **60** 085002
- [43] Estrada T. *et al* 2019 Turbulence and perpendicular plasma flow asymmetries measured at TJ-II plasmas *Nucl. Fusion* **59** 076021
- [44] Vermare L., Hennequin P., Gürçan O.D., Bourdelle C., Clairet F., Garbet X. and Sabot R. 2011 Impact of collisionality on fluctuation characteristics of micro-turbulence *Phys. Plasmas* **18** 012306
- [45] Estrada T. *et al* (The W7-X Team) 2021 Impact of magnetic islands on plasma flow and turbulence in W7-X *Nucl. Fusion* **61** 096011
- [46] Marushchenko N.B., Turkin Y. and Maassberg H. 2014 Ray-tracing code TRAVIS for ECR heating, EC current drive and ECE diagnostic *Comput. Phys. Commun.* **185** 165–76
- [47] Pasch E., Beurskens M.N., Bozhenkov S.A., Fuchert G., Knauer J. and Wolf R.C. 2016 The Thomson scattering system at Wendelstein 7-X *Rev. Sci. Instrum.* **87** 11E729
- [48] Hirshman S. 1983 Steepest-descent moment method for three-dimensional magnetohydrodynamic equilibria *Phys. Fluids* **26** 3553
- [49] Pablant N.A. *et al* 2018 Core radial electric field and transport in Wendelstein 7-X plasmas *Phys. Plasmas* **25** 022508
- [50] Windisch T., Krämer-Flecken A., Velasco J., Könies A., Nührenberg C., Grulke O. and Klinger T. 2017 Poloidal correlation reflectometry at W7-X: radial electric field and coherent fluctuations *Plasma Phys. Control. Fusion* **59** 105002
- [51] Bozhenkov S.A. *et al* 2017 The Thomson scattering diagnostic at Wendelstein 7-X and its performance in the first operation phase *J. Instrum.* **12** P10004
- [52] Happel T., Blanco E. and Estrada T. 2010 On the role of spectral resolution in velocity shear layer measurements by Doppler reflectometry *Rev. Sci. Instrum.* **81** 10D901
- [53] Laube R., Laux M., Ye M.Y., Greuner H. and Lindig S. 2011 Designs of Langmuir probes for W7-X *Fusion Eng. Des.* **86** 1133–6
- [54] Gao Y., Jakubowski M.W., Drewelow P., Pisano F., Puig Sitjes A., Niemann H., Ali A. and Cannas B. 2019 Methods for quantitative study of divertor heat loads on W7-X *Nucl. Fusion* **59** 066007
- [55] Herrmann A., Junker W., Gunther K., Bosch S., Kaufmann M., Neuhauser J., Pautasso G., Richter T. and Schneider R. 1995 Energy flux to the ASDEX-upgrade divertor plates determined by thermography and calorimetry *Plasma Phys. Control. Fusion* **37** 17–29
- [56] Li Y. *et al* (The W7-X Team) 2019 Measurement of the edge ion temperature in W7-X with island divertor by a retarding field analyzer probe *Nucl. Fusion* **59** 126002
- [57] Stangeby P. 2000 *The Plasma Boundary of Magnetic Fusion Devices* 1st edn (Boca Raton, FL: CRC Press)
- [58] Brida D. *et al* 2017 Heat flux pattern in detached L-modes and ELM mitigated H-modes with rotating magnetic perturbations in ASDEX upgrade *Nucl. Fusion* **57** 116006
- [59] Gao Y. *et al* 2020 Understanding baffle overloads observed in high-mirror configuration on Wendelstein 7-X *Nucl. Fusion* **60** 096012
- [60] Wolf R.C. *et al* 2017 Major results from the first plasma campaign of the Wendelstein 7-X stellarator *Nucl. Fusion* **57** 102020

- [61] Carralero D. *et al* 2021 An experimental characterization of core turbulence regimes in Wendelstein 7-X *Nucl. Fusion* **61** 096015
- [62] Perseo V., Effenberg F., Gradic D., König R., Ford O., Reimold F., Ennis D., Schmitz O. and Sunn Pedersen T. 2019 Direct measurements of counter-streaming flows in a low-shear stellarator magnetic island topology *Nucl. Fusion* **59** 124003
- [63] Kriete M. *et al* 2022 Effects of drifts on scrape-off layer transport in the W7-X stellarator *64th Annual Meeting of the American Physical Society (Auburn, USA, 17th–21st October 2022)* (available at: <http://w7-x.auburn.edu/presentations/>)
- [64] Jakubowski M. *et al* (The W7-X Team) 2021 Overview of the results from divertor experiments with attached and detached plasmas at Wendelstein 7-X and their implications for steady-state operation *Nucl. Fusion* **61** 106003
- [65] Zoletnik S. *et al* 2018 Advanced neutral alkali beam diagnostics for applications in fusion research (invited) *Rev. Sci. Instrum.* **89** 10D107
- [66] Windisch T. *et al* 2022 Doppler reflectometry system upgrades for Wendelstein 7-X OP2 *23rd Int. Stellarator Heliotron Workshop (Warsaw, Poland, 20th–24th June 2022)* (available at: [www.ifpilm.pl/ishw2022](http://www.ifpilm.pl/ishw2022))